Earth and Planetary Science Letters 447 (2016) 139–150

Contents lists available at ScienceDirect

Earth and Planetary Science Letters

www.elsevier.com/locate/epsl

Exploring the scale-dependent permeability of fractured andesite

Michael J. Heap [a,*], Ben M. Kennedy [b]

[a] Géophysique Expérimentale, Institut de Physique de Globe de Strasbourg (UMR 7516 CNRS, Université de Strasbourg/EOST), 5 rue René Descartes, 67084 Strasbourg cedex, France

[b] Department of Geological Sciences, University of Canterbury, Private Bag 4800, Christchurch, New Zealand

ARTICLE INFO

Article history:
Received 21 November 2015
Received in revised form 10 March 2016
Accepted 3 May 2016
Available online 19 May 2016
Editor: T.A. Mather

Keywords:
volcano
outgassing
porosity
equivalent permeability
upscaling

ABSTRACT

Extension fractures in volcanic systems exist on all scales, from microscopic fractures to large fissures. They play a fundamental role in the movement of fluids and distribution of pore pressure, and therefore exert considerable influence over volcanic eruption recurrence. We present here laboratory permeability measurements for porous (porosity = 0.03–0.6) andesites before (i.e., intact) and after failure in tension (i.e., the samples host a throughgoing tensile fracture). The permeability of the intact andesites increases with increasing porosity, from 2×10^{-17} to 5×10^{-11} m^2. Following fracture formation, the permeability of the samples (the equivalent permeability) falls within a narrow range, $2–6 \times 10^{-11}$ m^2, regardless of their initial porosity. However, laboratory measurements on fractured samples likely overestimate the equivalent permeability due to the inherent scale-dependence of permeability. To explore this scale-dependence, we first determined the permeability of the tensile fractures using a two-dimensional model that considers flow in parallel layers. Our calculations highlight that tensile fractures in low-porosity samples are more permeable (as high as 3.5×10^{-9} m^2) than those in high-porosity samples (as low as 4.1×10^{-10} m^2), a difference that can be explained by an increase in fracture tortuosity with porosity. We then use our fracture permeability data to model the equivalent permeability of fractured rock (with different host rock permeabilities, from 10^{-17} to 10^{-11} m^2) with increasing lengthscale. We highlight that our modelling approach can be used to estimate the equivalent permeability of numerous scenarios at andesitic stratovolcanoes in which the fracture density and width and host rock porosity or permeability are known. The model shows that the equivalent permeability of fractured andesite depends heavily on the initial host rock permeability and the scale of interest. At a given lengthscale, the equivalent permeability of high-permeability rock (10^{-12} to 10^{-11} m^2) is essentially unaffected by the presence of numerous tensile fractures. By contrast, a single tensile fracture increases the equivalent permeability of low-permeability rock ($<10^{-15}$ m^2) by many orders of magnitude. We also find that fractured, low-permeability rock (e.g., 10^{-17} m^2) can have an equivalent permeability higher than that of similarly fractured rock with higher host rock permeability (e.g., 10^{-15} m^2) due to the low-tortuosity of fractures in low-porosity andesite. Our modelling therefore outlines the importance of fractures in low-porosity, low-permeability volcanic systems. While our laboratory measurements show that, regardless of the initial porosity, the equivalent permeability of fractured rock on the laboratory scale is $2–6 \times 10^{-11}$ m^2, the equivalent permeability of low-permeability rock is significantly reduced as the scale of interest is increased. Therefore, due to the scale-dependence of permeability, laboratory measurements on pristine, low-permeability rocks significantly underestimate the equivalent permeability of fractured volcanic rock. Further, measurements on fractured rock samples can significantly overestimate the equivalent permeability. As a result, care must be taken when selecting samples in the field and when using laboratory data in volcano outgassing models. The data and modelling presented herein provide insight into the scale-dependence of the permeability of fractured volcanic rock, a prerequisite for understanding outgassing at active volcanoes.

1. Introduction

Extension fractures (tensile fractures and hydrofractures) are ubiquitous in volcanic systems, a consequence of the mechani-

* Corresponding author.
E-mail address: heap@unistra.fr (M.J. Heap).

http://dx.doi.org/10.1016/j.epsl.2016.05.004

cal (e.g., Heiken et al., 1988) and thermal stresses (e.g., Aydin and DeGraff, 1988) inherent to these environments and the low tensile strength of rock (strength in tension is typically an order of magnitude lower than compressive strength; Jaeger et al., 2007). Extension fractures commonly seen within volcano environments include: microscopic cooling fractures (e.g., Heap et al., 2014), macroscopic polygonal cooling fractures in lavas and lava domes (e.g., Aydin and DeGraff, 1988; Spörli and Rowland, 2006), hydrofractures and tuffisites (e.g., Knapp and Knight, 1977; Heiken et al., 1988; Stasiuk et al., 1996; Sparks, 1997; Tuffen and Dingwell, 2005; Kolzenburg et al., 2012; Castro et al., 2014), crease structures (e.g., Anderson and Fink, 1992), lava dome fractures that form due to a combination of subsurface overpressures and regional stresses (such as that formed following the 2013 explosion at Mt. Merapi, Indonesia; Walter et al., 2015), and large crevasses/fissures (e.g., Gudmundsson, 2011; Fitzgerald et al., 2014). In many cases, magma fragmentation in conduits is dominated by extension fractures with a wide range of orientations (Kennedy et al., 2005). Extension fractures form due to the high overpressures generated by exsolving magmatic fluids, the thermal expansion of pore fluids, and/or the magmatic stresses (hydrofractures; e.g., Knapp and Knight, 1977; Heiken et al., 1988; Benson et al., 2012) or simply as a result of the tensile stresses exceeding the local tensile strength (tensile fractures; e.g., see the experiments presented in Lavallée et al., 2012). Both mechanisms require that, if the temperature exceeds the glass transition of the melt phase *Tg*, strain rates are high enough to exceed the structural relaxation timescale of the melt (Dingwell and Webb, 1990).

The extension fractures outlined above occur on a wide range of scale, from the microscale (Fig. 1a shows a back-scattered scanning electron photomicrograph of a cooling microcrack within one of the andesite samples of this study) to the hand sample or laboratory-scale (Fig. 1b shows a photograph of a block collected from Volcán de Colima (Mexico) containing a tensile fracture; inset shows a cylindrical laboratory sample (20 mm in diameter and 40 mm in length) prepared from the block) to the meso- or outcrop-scale (Fig. 1c shows columnar cooling fractures at Mt. Ruapehu, New Zealand) to, finally, the macroscale (Fig. 1d shows the fissure exposed following the 2012 eruption from the Te Maari vent at Mt Tongariro, New Zealand). Once formed, extension fractures principally perform two functions at active volcanoes: (1) they reduce the structural stability of the volcano and lava dome (e.g., Voight, 2000) and, (2) they act as pathways for fluids. The ease with which exsolved magmatic gases can escape the conduit—governed by the permeability of the rock and magma—is thought to impact volcanic explosivity (as discussed by many authors, e.g., Eichelberger et al., 1986; Sparks, 1997; Mueller et al., 2005; Melnik et al., 2005; Edmonds and Herd, 2007; Lavallée et al., 2013; Castro et al., 2014). Extension fractures in particular are considered to be a key component in facilitating the outgassing of the conduit magma (e.g., Castro et al., 2014). Indeed, overpressure-driven fractures can propagate to considerable distances and are thought to form efficient fluid pathways (Heiken et al., 1988; Gudmundsson et al., 2002).

Laboratory studies designed to measure the impact of tensile fracture formation on permeability are few, especially for volcanic rocks. Well-constrained laboratory measurements have shown that sample-scale tensile fractures increase permeability of very low-porosity basalt (porosity <0.05) and porous andesite (porosity $=$ 0.17–0.18) by many orders of magnitude (Nara et al., 2011) and by a factor of almost two (Heap et al., 2015a), respectively. The few number of studies, and the discrepancy between measurements performed on rock with different porosity (Nara et al., 2011; Heap et al., 2015a), highlight the need for systematic laboratory studies to better understand the influence of tensile fractures on the permeability of variably-porous volcanic rock. How-

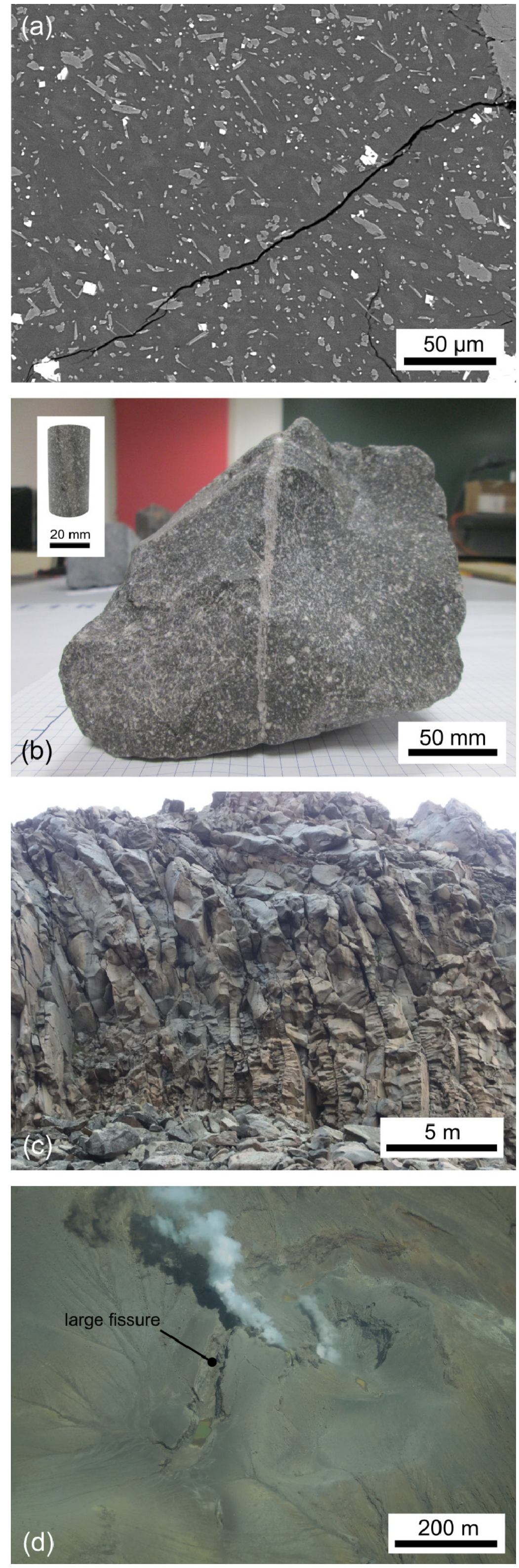

Fig. 1. A voyage through scales. (a) A microscopic cooling fracture in one of the andesites of this study (sample R10). The fracture, seen here to cut through a glassy groundmass containing microlites, is only a few microns wide. (b) A hand- or laboratory-scale block (roughly $20 \times 20 \times 20$ cm) of andesite from Volcán de Colima (Mexico) containing a fracture. The fracture is a couple of mm wide. Inset shows a cylindrical laboratory sample cored from the block shown (20 mm in diameter and 40 mm in length). (c) Macroscopic polygonal columnar cooling fractures in an outcrop at Mt. Ruapehu (New Zealand). Photo credit: Ben Kennedy. (d) Aerial photograph of the large fissure formed following the 2012 eruption from the Te Maari vent at Tongariro (New Zealand). Photo credit: Tetsuo Kobayashi.

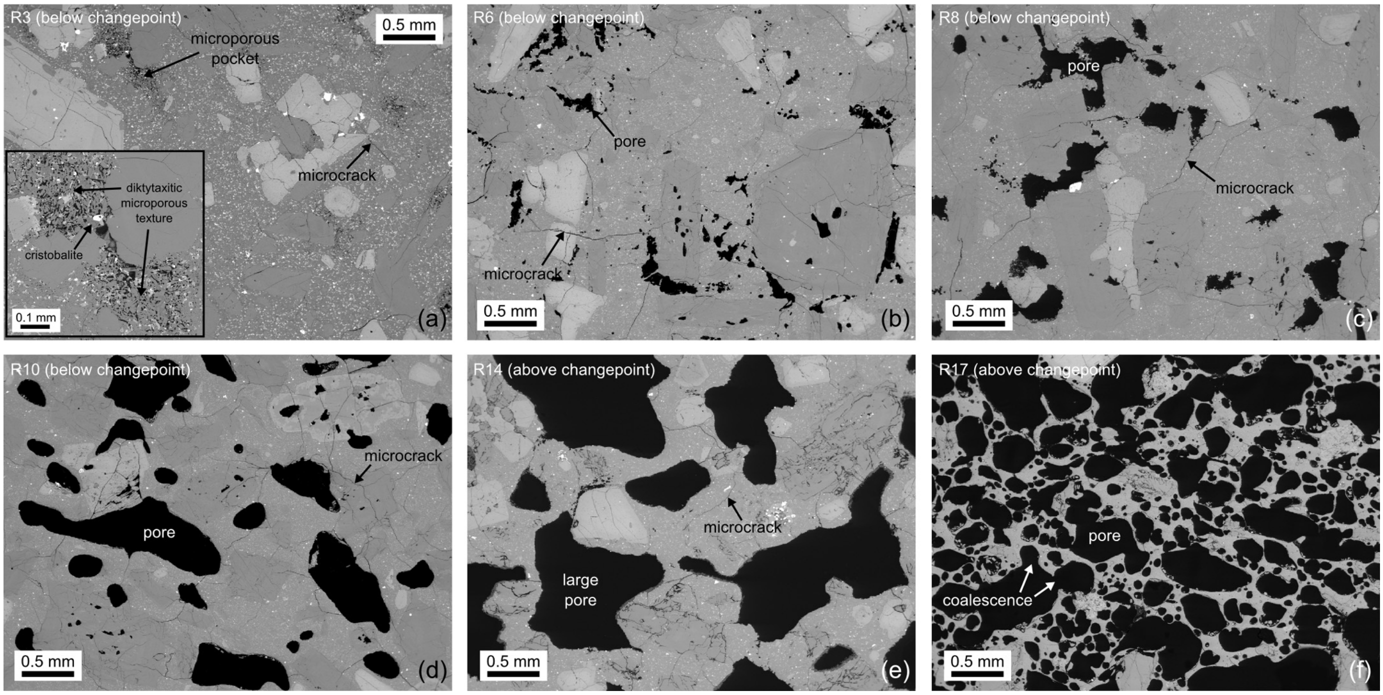

Fig. 2. Intact microstructure. Back-scattered electron microscope images of some of the andesites of this study, arranged from low to high porosity. (a) Image of sample R3 ("altered lava"). A microporous pocket and a microcrack are labelled on the image. The inset shows a zoomed-in image of one of the microporous pockets; diktytaxitic microtextures and "fish-scale" cristobalite are labelled on the inset. (b–e) Images of samples R6, R8, R10, and R14 ("lavas"). A pore and a microcrack are labelled on each of the images. (f) Image of sample R17 ("scoracious"). A pore and pore coalescence are labelled on the image.

ever, while well-constrained laboratory measurements offer considerable insight, it is well known that permeability exhibits a scale effect (Brace, 1984; Clauser, 1992; Neuman, 1994). Laboratory measurements on pristine samples do not account for meso- and macroscale fractures (Figs. 1c and 1d) and therefore underestimate the equivalent permeability of rock (e.g., Clauser, 1992). Similarly, laboratory measurements on samples containing heterogeneities (such as fractures and layering; Fig. 1b) will likely under- or overestimate the equivalent permeability of rock depending on whether the feature(s) serves as a barrier to flow or a conduit for flow, respectively. The extrapolation of laboratory data to larger scales is an outstanding challenge in volcanology. Currently, such extrapolations for fractured volcanic rock are hampered by the paucity of well-constrained laboratory data.

Our aim here is to explore upscaling in fractured andesites using a new laboratory dataset. We first present new laboratory measurements of permeability for a suite of variably-porous (porosity = 0.03–0.6) andesites before and after the formation of a macroscopic tensile (extension) fracture. We use these data to extract the permeability of the fractures, which are then used to explore the role of lengthscale on the equivalent permeability of rock using a two-dimensional model that considers flow in parallel layers. A grasp of the scale-dependence of the permeability of fractured volcanic rock is a prerequisite for understanding and modelling outgassing at active volcanoes (e.g., Collombet, 2009; Collinson and Neuberg, 2012).

2. Materials and methods

A suite of variably porous andesites was selected for this study. The andesite blocks (roughly 10 × 10 × 10 cm in size) were collected on the northern flank of Mt. Ruapehu—an active stratovolcano at the southern end of the Taupo Volcanic Zone (TVZ) in New Zealand's North Island—and are all part of the Whakapapa Formation, the youngest of the units that comprise the present-day edifice (Hackett and Houghton, 1989). Although the materials are sourced from the edifice of Mt. Ruapehu, the data presented in this study are likely applicable to other active andesitic stratovolcanoes, such as Volcán de Colima, Soufrière Hills (Montserrat), Merapi, Santa María (Guatemala), and Tungurahua (Ecuador). Fifteen blocks were collected in total: four "altered lavas", ten "lavas", and one "scoracious" sample (using the classification scheme of Farquharson et al., 2015). We note that none of the blocks contained fractures visible to the naked eye. The microstructure of samples selected to best represent the measured range in porosity is presented in Fig. 2. We find that the porosity in the low-porosity (0.03–0.04) altered sample is not distributed throughout the sample, but exists as pockets of microporosity commonly sandwiched between crystals (Fig. 2a). This microporous texture—termed diktytaxitic (Kushnir et al., 2016 and references therein)—is associated with cristobalite (a high-temperature, low-pressure silica polymorph; Deer et al., 1992), identifiable by its characteristic fish-scale texture (Deer et al., 1992) (see inset in Fig. 2a). Photomicrographs of the lava samples show that the increase in porosity is coupled with an increase in the pore diameter; the lava samples are also pervasively microcracked (Figs. 2b–e). The microstructure of the scoracious sample is characterised by a bimodal distribution of sub-equant pores, with peaks at diameters of about 100 μm and 500 μm (Fig. 2f). The scoracious sample also shows evidence of bubble coalescence (Fig. 2f).

Two cylindrical samples, 20 mm in diameter and precision-ground flat and parallel to a nominal length of 20 mm (length to width ratios lower than one are not recommended for laboratory permeability measurements), were prepared from each of the fifteen blocks collected (apart from sample R15, for which there is only one sample). 29 samples were prepared in total: 8 altered lava samples, 19 lava samples, and 2 scoracious samples (using the classification scheme of Farquharson et al., 2015) (see Tables 1 and 2). The connected porosity of each sample was measured using a helium pycnometer. Their initial, pre-fracture gas (nitrogen) permeability was measured using a benchtop steady-state permeameter (Figs. 3a and 3b). All measurements were conducted under

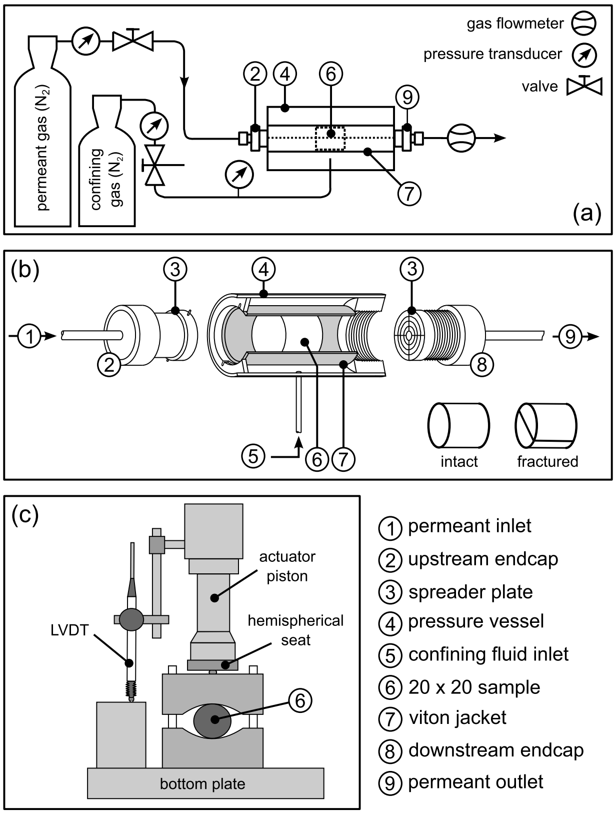

Fig. 3. Schematics of the experimental apparatus. (a–b) Schematic diagrams (not to scale) of the benchtop permeameter. Inset in panel (b) shows a schematic of an intact sample and a fractured sample showing the geometry of the fracture plane. (c) Schematic diagram (not to scale) of the uniaxial load frame used to deform the samples.

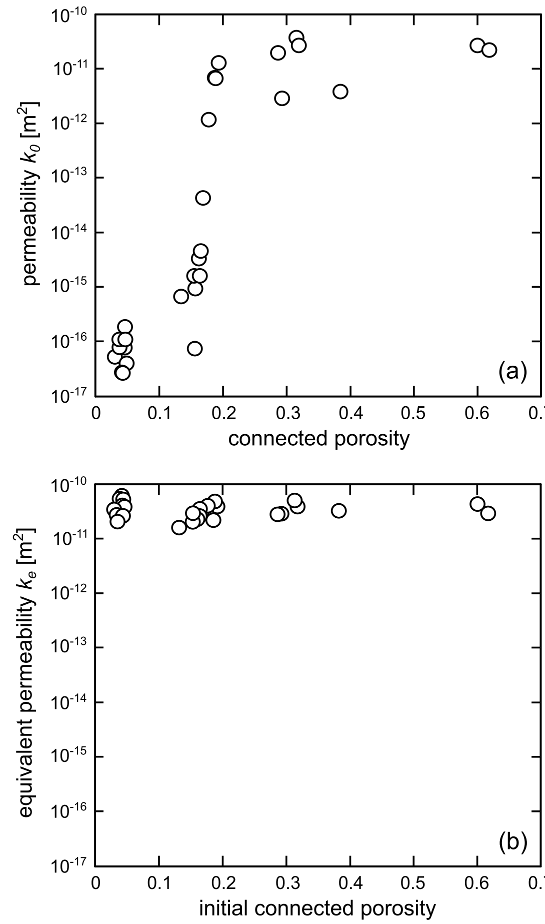

Fig. 4. Laboratory measurements. (a) Intact permeability (k_0) as a function of connected porosity. (b) Equivalent permeability (k_e) of the fractured samples as a function of initial connected porosity. Experimental error is captured by the symbol size.

a confining pressure of 1 MPa. Flow rate measurements were taken (using either a low- or high-flow gas flowmeter, depending on the permeability of the sample) under several pressure gradients (typically from 0.05 to 0.2 MPa, equating to flow rates between 0.2 and 400 ml/min) to determine the permeability using Darcy's law and to assess the need for the Klinkenberg or Forchheimer corrections, which were applied on a case-by-case basis. The samples were then double-wrapped in tape and loaded diametrically in compression (at a constant displacement rate of 0.004 mm/s) until tensile failure using a servo-controlled uniaxial load frame (Fig. 3c). The samples were unloaded following the formation of the first macrofracture (a throughgoing tensile fracture in each case) and their post-fracture permeability was measured using the same procedure described above. The plane of the throughgoing fracture was oriented parallel to the direction of fluid flow (see inset in Fig. 3b). While the fracture experiments yielded a load at failure, indirect tensile strengths are not reported here because the diameter of our samples does not meet the recommended minimum requirement (54 mm) of the International Society of Rock Mechanics (Ulusay and Hudson, 2007). All experiments and measurements were conducted on dry samples (dried in a vacuum oven at 40 °C for a minimum of 48 h) at room temperature.

3. Results

Measured values of intact (pre-fracture) permeability are plotted as a function of connected porosity in Fig. 4a. Intact permeability k_0 increases as connected porosity increases (Fig. 4a). In detail, permeability was measured to be between $1\text{–}2 \times 10^{-16}$ and 2×10^{-17} m^2 at the lowest porosities of 0.03–0.04 and to be about 5×10^{-11} m^2 at the highest porosity of 0.6 (Fig. 4a; Tables 1 and 2). A single power law cannot describe the porosity–permeability trend on the log-linear graph of Fig. 4a: permeability increases significantly as porosity is increased from 0.03 to about 0.18–0.19, while the increase in permeability between a porosity of about 0.18–0.19 and 0.6 is modest. The permeability of the samples following the formation of a macroscopic tensile fracture—termed here the equivalent permeability k_e (Renard and de Marsily, 1997)—is plotted as a function of initial connected porosity in Fig. 4b. The equivalent permeabilities of all the fractured samples fall within a narrow range, $2\text{–}6 \times 10^{-11}$ m^2, regardless of the initial porosity (Fig. 4b; Tables 1 and 2).

4. Discussion

4.1. Porosity–permeability relationships

The nonlinearity in the porosity–permeability trend of volcanic rock has been considered by some authors to be well captured by a single power law model (e.g., Mueller et al., 2005). Recently however, Bayesian Information Criterion (BIC) analysis has revealed that the porosity–permeability trend for some volcanic materials is better described by two or more discrete power law models that intersect at so-called "porosity changepoints" x^* (Farquharson et al., 2015; Heap et al., 2015b; Kushnir et al., 2016). These changepoints are thought to exist due to microstructural differences between high- and low-porosity volcanic materials. For example, low-porosity rocks (below about 0.15) often contain a poorly-connected or tortuous network of pores, and fluids are often obliged to travel through narrow microcracks that

Table 1
Summary of the laboratory data collected for this study below the microstructural changepoint. AL—"altered lava"; L—"lava". Fracture permeabilities were calculated using Equation (2). The intact area A_{intact} used in Equation (2) was taken as the sample area A (calculated using the sample width W) minus the fracture area $A_{fracture}$ (calculated using the fracture length and a fracture width of 0.25 mm).

Sample	Sample width W (mm)	Connected porosity	Confining pressure (MPa)	Pre-fracture permeability k_0 (m^2)	Post-fracture permeability k_e (m^2)	Fracture length (mm)	Fracture permeability k_f (m^2)
R1 T1 (AL)	20.00	0.043	1	2.63×10^{-17}	6.10×10^{-11}	20.87	1.75×10^{-9}
R1 T2 (AL)	19.99	0.041	1	2.74×10^{-17}	5.08×10^{-11}	20.55	3.10×10^{-9}
R2 T1 (AL)	19.99	0.038	1	1.09×10^{-16}	2.34×10^{-11}	21.12	1.39×10^{-9}
R2 T2 (AL)	20.00	0.031	1	5.23×10^{-17}	3.31×10^{-11}	20.52	2.03×10^{-9}
R3 T1 (AL)	20.00	0.047	1	3.87×10^{-17}	2.46×10^{-11}	21.06	1.47×10^{-9}
R3 T2 (AL)	19.99	0.048	1	3.96×10^{-17}	3.56×10^{-11}	20.97	2.13×10^{-9}
R4 T1 (AL)	20.01	0.046	1	1.87×10^{-16}	4.51×10^{-11}	20.59	2.76×10^{-9}
R4 T2 (AL)	20.01	0.045	1	7.65×10^{-17}	5.75×10^{-11}	20.73	3.49×10^{-9}
R6 T1 (L)	20.00	0.038	1	7.92×10^{-17}	1.97×10^{-11}	21.67	1.14×10^{-9}
R6 T2 (L)	20.00	0.047	1	1.11×10^{-16}	3.83×10^{-11}	20.72	2.32×10^{-9}

Table 2
Summary of the laboratory data collected for this study above the microstructural changepoint. L—"lava"; S—"scoracious". Fracture permeabilities were calculated using Equation (2). The intact area A_{intact} used in Equation (2) was taken as the sample area A (calculated using the sample width W) minus the fracture area $A_{fracture}$ (calculated using the fracture length and a fracture width of 0.25 mm).

Sample	Sample width W (mm)	Connected porosity	Confining pressure (MPa)	Pre-fracture permeability k_0 (m^2)	Post-fracture permeability k_e (m^2)	Fracture length (mm)	Fracture permeability k_f (m^2)
R7 T1 (L)	20.01	0.193	1	1.32×10^{-11}	3.70×10^{-11}	20.96	1.44×10^{-9}
R7 T2 (L)	20.00	0.188	1	6.71×10^{-12}	4.82×10^{-11}	21.47	2.44×10^{-9}
R8 T1 (L)	20.02	0.155	1	1.62×10^{-15}	1.94×10^{-11}	21.77	1.12×10^{-9}
R8 T2 (L)	20.02	0.162	1	3.34×10^{-15}	2.20×10^{-11}	21.32	1.30×10^{-9}
R9 T1 (L)	20.01	0.157	1	9.21×10^{-16}	2.95×10^{-11}	22.68	1.64×10^{-9}
R9 T2 (L)	20.01	0.156	1	7.35×10^{-17}	2.97×10^{-11}	21.11	1.77×10^{-9}
R10 T1 (L)	20.01	0.134	1	6.71×10^{-16}	1.62×10^{-11}	21.37	9.53×10^{-10}
R10 T2 (L)	20.02	0.163	1	1.62×10^{-15}	2.56×10^{-11}	21.46	1.50×10^{-9}
R11 T1 (L)	19.99	0.169	1	4.33×10^{-14}	2.79×10^{-11}	21.81	1.60×10^{-9}
R11 T2 (L)	20.00	0.165	1	4.60×10^{-15}	3.37×10^{-11}	21.47	1.97×10^{-9}
R12 T1 (L)	20.02	0.187	1	6.85×10^{-12}	2.21×10^{-11}	22.09	8.76×10^{-10}
R12 T2 (L)	20.03	0.178	1	1.19×10^{-12}	3.99×10^{-11}	21.88	2.23×10^{-9}
R13 T1 (L)	19.98	0.293	1	2.89×10^{-12}	2.81×10^{-11}	22.05	1.44×10^{-9}
R13 T2 (L)	20.00	0.287	1	1.98×10^{-11}	2.80×10^{-11}	22.27	4.82×10^{-10}
R14 T1 (L)	20.01	0.384	1	3.89×10^{-12}	3.20×10^{-11}	22.96	1.54×10^{-9}
R14 T2 (L)	19.99	0.316	1	3.97×10^{-11}	4.92×10^{-11}	23.59	5.45×10^{-10}
R15 T1 (L)	19.99	0.319	1	2.72×10^{-11}	3.86×10^{-11}	21.72	6.86×10^{-10}
R17 T1 (S)	20.00	0.600	1	2.74×10^{-11}	4.40×10^{-11}	23.33	9.21×10^{-10}
R17 T2 (S)	19.97	0.618	1	2.25×10^{-11}	2.95×10^{-11}	22.58	4.11×10^{-10}

connect the pore network (Heap et al., 2014; Farquharson et al., 2015; Kushnir et al., 2016). Moderate- to high-porosity rocks (above about 0.15), by contrast, often contain a well-connected network of large pores and channels (Rust and Cashman, 2004; Wright et al., 2006; Farquharson et al., 2015; Kennedy et al., 2015; Kushnir et al., 2016). The break-in-slope in the data presented in Fig. 4a also suggests a changepoint porosity, which was calculated using BIC analysis to be at a porosity of 0.19 (Fig. 5a). Data from the altered lavas, and low-porosity lava sample R6, were excluded from our BIC analysis. Kushnir et al. (2016) also found that andesites containing porosities below 0.05 do not align with a model containing two power laws. In our data, while these low-porosity samples could indicate the presence of another porosity changepoint at a porosity between 0.11–0.15 (with the data described by a power law with a low exponent), we highlight that most of these samples contain complex microstructures due to low-pressure, high-temperature alteration (Fig. 2a; Kushnir et al., 2016) and that we have insufficient data to draw firm conclusions. The existence of a changepoint in the rocks presented here is interpreted as a change in void space connectivity at a porosity of 0.19, the same conclusion drawn by previous authors (Farquharson et al., 2015; Heap et al., 2015b; Kushnir et al., 2016). This interpretation is supported by microstructural observations: rocks below the changepoint contain few pores and a pervasive microcrack network (thought to be a consequence of their cooling history, as previously inferred for similar edifice-forming andesites; Heap et al. (2014)) (Figs. 2b–d), while rocks above the changepoint contain a dense network of large pores (Figs. 2e–f).

4.2. Modelling the equivalent permeability of rock containing tensile fractures

A fundamental model for flow through a fracture is the parallel plate model, which assumes that the fracture walls are smooth, parallel plates separated by a fracture of width h. The derivation of this model yields an exact solution for fracture permeability k_f (Zimmerman and Bodvarsson, 1996):

$$k_f = \frac{h^2}{12} \tag{1}$$

Constraining the width of our experimental fractures is challenging however. While the width of the fractures varies little between different samples of varying porosity (Figs. 5b and 5c), a fracture within a particular sample can vary from ∼0.1 to ∼0.6 mm (Fig. 5c). Further, our permeability measurements were conducted at a confining pressure of 1 MPa, and therefore the crack width associated with the permeability measurement may be lower than that depicted in Figs. 5b and 5c. Additionally, fracture width may vary along its plane. Since we cannot well constrain our fracture

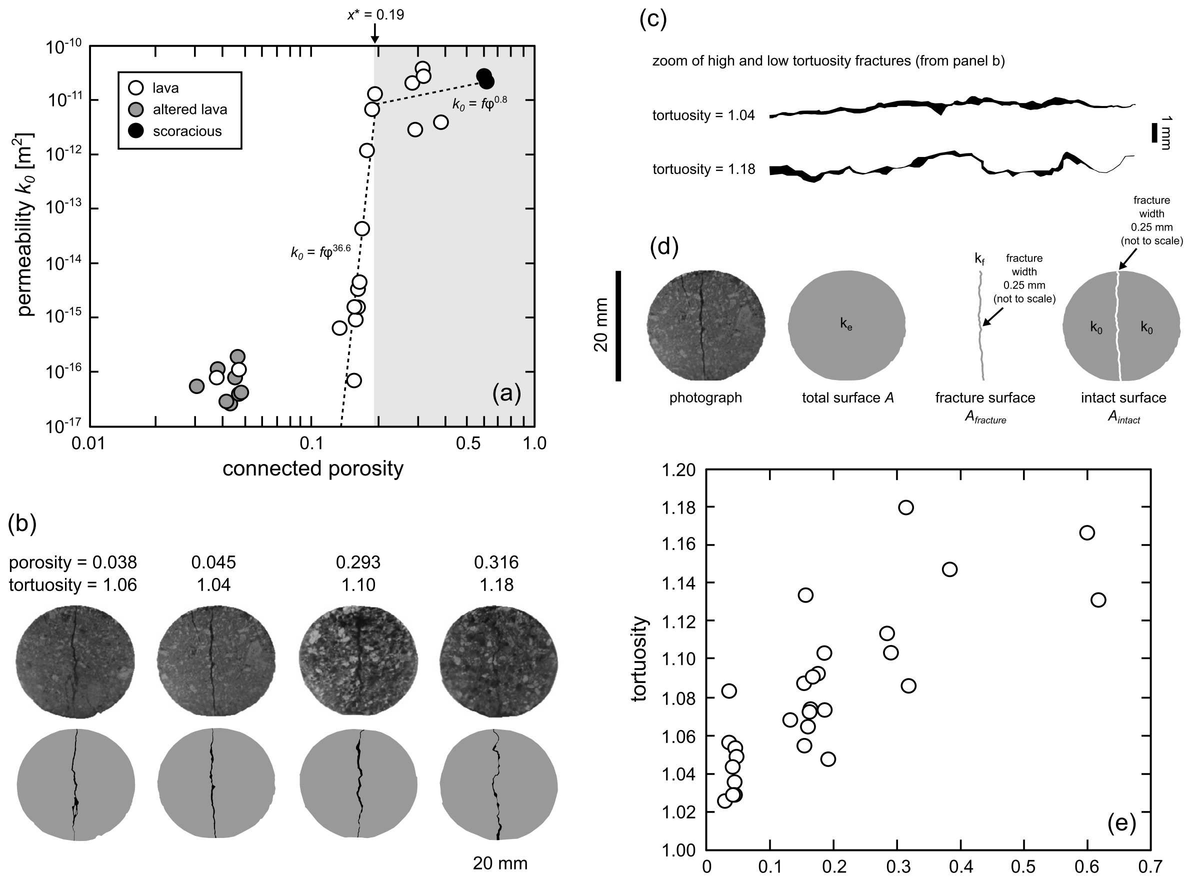

Fig. 5. (a) Microstructural changepoint. Log–log plot of intact permeability (k_0) as a function of connected porosity (i.e., the data of Fig. 4a). Best-fit slopes provided by the Bayesian Information Criterion (BIC) method are also shown (see text for details). The power law exponent for each of the slopes is provided next to the relevant curve. The colour of each data point corresponds to the classification of the sample (using the classification scheme of Farquharson et al., 2015). White—lava. Grey—altered lava. Black—scoracious. The porosity changepoint x^* is labelled on the figure, those points above and below the changepoint lie in the grey and white zones, respectively. (b) Examples of the tensile fractures formed in the experimental samples (top—photograph of the end face of the sample; bottom—schematic diagram of the sample with the main fracture indicated), ordered from low to high porosity. (c) Magnified images of two of the fractures shown in panel (b), the least and most tortuous fracture. (d) Model setup for the determination of fracture permeability using Equation (2) (see text for details). Surface in question is indicated in grey. k_0 = intact permeability, k_f = fracture permeability, and k_e = equivalent permeability. (e) Fracture tortuosity as a function of initial connected porosity.

widths at our experimental pressure, we will assume a conservative and constant fracture width of 0.25 ± 0.1 mm for all of the fractures. Assuming a constant h of 0.25 ± 0.1 mm, Equation (1) yields a fracture permeability of $2.08 \times 10^{-8} \pm 8.33 \times 10^{-12}$ m^2. Inspection of our experimental samples reveals however that the assumption of smooth, parallel fracture walls is invalid (Fig. 5c). Generally speaking, rough-walled fractures are less permeable than fractures with smooth walls (e.g., Brown, 1987; Thompson and Brown, 1991; Zimmerman et al., 1992). Better estimations of the permeability of fractures with more realistic geometries are possible using the contact surface area of the fracture surfaces (Zimmerman and Bodvarsson, 1996). However, and due to the difficulty in measuring the contact surface (especially under a confining pressure), we adopt here a different approach that interrogates our new experimental dataset.

If we consider the permeability of a sample containing a fracture as an equivalent permeability (k_e), we can extract the fracture permeability (k_f) using the following two-dimensional model that considers flow in parallel layers (a fracture between two layers of host rock):

$$k_f = \frac{Ak_e - A_{intact} \cdot k_0}{A_{fracture}} \tag{2}$$

Where k_0 is the intact permeability and A is the area of the sample end face. A can be subdivided into the area of fracture ($A_{fracture}$) and the area of intact rock (A_{intact}). The model setup is shown in Fig. 5d. k_0 and k_e were measured for each rock, and we determine A using the measured sample diameter (Tables 1 and 2). Calculating $A_{fracture}$ requires the length and width of each fracture. While we assume a fixed value of fracture width (0.25 ± 0.1 mm) for this calculation (see reasoning above), we note that the fracture length, which varies between the samples (Figs. 5b and 5c), will not be modified upon the application of a 1 MPa confining pressure. The fracture length, which was measured on the end face of each sample (Figs. 5b and 5c; Tables 1 and 2), also defines a fracture tortuosity. If we plot fracture tortuosity as a function of the initial connected porosity we find that the tortuosity of a tensile fracture increases as the initial connected porosity is increased (Fig. 5e). The path of tensile fractures in the higher porosity samples is influenced by the distribution of large diameter pores; in our samples, pore size tends to increase with porosity (see Figs. 2b–d). In the low-porosity samples, the stress field is not perturbed by the presence of large pores and the fracture is much straighter as a result (Figs. 5b and 5c). We highlight that our model assumes that the fracture area and tortuosity at the end face of the sample is representative of the internal geometry of the fracture in a particular sample. The intact area A_{intact} used in Equation (2) was simply taken as the sample area A minus the fracture area $A_{fracture}$ (all of the values required for the calculation of k_f are provided in Tables 1 and 2). Fracture permeability

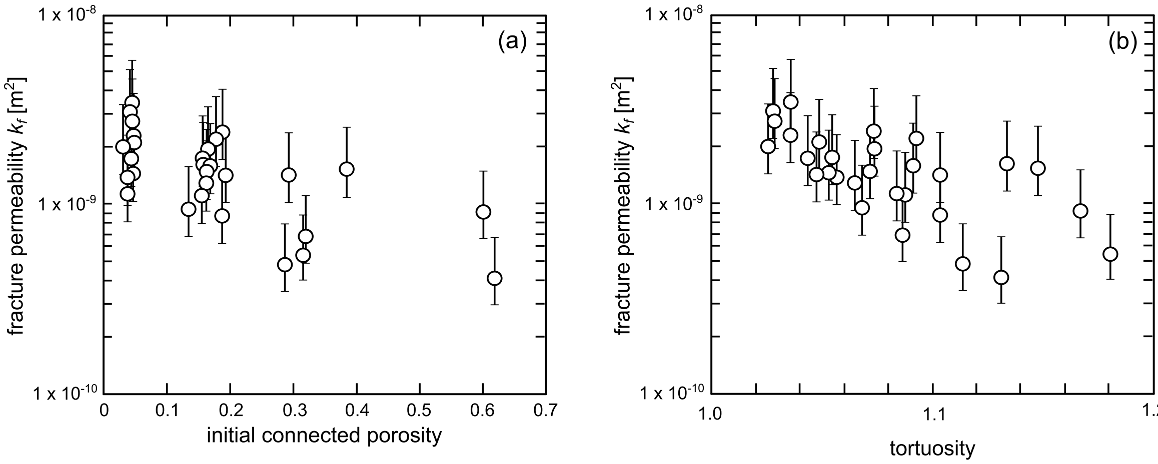

Fig. 6. Tensile fracture permeability (k_f), calculated using Equation (2), as a function of (a) initial connected porosity and (b) fracture tortuosity. Error bars represent the anticipated variability of the fracture width at a confining pressure of 1 MPa (0.25 ± 0.1 mm) (see text for details).

k_f (determined using Equation (2)) is plotted as a function of initial connected porosity and fracture tortuosity in Figs. 6a and 6b, respectively (the error bars account for the anticipated variability of the fracture width, 0.25 ± 0.1 mm). Our data show that fracture permeability decreases as the initial connected porosity (Fig. 6a) or tortuosity increases (Fig. 6b). Our calculated fracture permeabilities are all lower (some by a couple of orders of magnitude) than that predicted using Equation (1) for smooth, parallel fracture walls.

Using our fracture permeability data (Tables 1 and 2), we can model the equivalent permeability of a given length of rock (with chosen host rock permeability) containing a 0.25 mm-wide tensile fracture using the following one-dimensional relation:

$$k_e = \frac{(w_{intact} \cdot k_0) + (w_{fracture} \cdot k_f)}{W} \tag{3}$$

Where W is the total rock width considered, which is subdivided into the width of the fracture $w_{fracture}$ and the width of the intact rock w_{intact}. The model setup is provided as an inset in Fig. 7a. Since fracture permeability decreases with increasing initial connected porosity (Fig. 6a), values of k_f for a given host rock permeability were determined using the empirical power law relationship between the initial permeability and fracture permeability. Our model not only allows us to consider a single fracture: we can increase the number of fractures in a given length of rock by increasing $w_{fracture}$ accordingly. We can now explore the influence of lengthscale on the equivalent permeability of fractured andesitic rock.

There are a few important upscaling considerations however. (1) Although increasing $w_{fracture}$ also allows us to increase the width of the fracture(s), we highlight that this extrapolation may not be appropriate. First, it is unclear whether heterogeneities on the mm-scale (pores and/or crystals) will influence the tortuosity of wider fractures; the tortuosity of larger fractures is likely a product of meso- or macro-scale heterogeneities. Second, an increase in fracture width will likely lead to changes in flow inertia. As a result, the upscaling of laboratory data to wide fissures (e.g., Fig. 1d) will likely require further consideration. Therefore, we restrict our modelling to rock containing one or more 0.25 mm-wide tensile fractures. (2) Fractures observed in the field are often wider than 0.25 mm (e.g., Gudmundsson, 2011). While this may restrict our upscaling discussion to short lengthscales for shallow rock (fluid flow at long lengthscales are likely controlled by fractures wider than those modelled herein), we highlight that wide fractures may not exist at depth unless they are propped open by, for example, high pore fluid pressures (e.g., Rust et al., 2004). Therefore, while the relevance of discussing lengthscales up to 100 m may be brought into question for subsurface fluid flow (or for zones where wide fractures are propped open), upscaling to long lengthscales (∼100 m) may be relevant for the equivalent permeability of fractured rock at depths where the lithostatic pressure inhibits the presence of wide fractures.

If we consider a 10 m length of rock (Fig. 7a), we find that the increase in equivalent permeability with number of tensile fractures (i.e., fracture density) depends heavily on the permeability of the host rock. We also highlight that these modelled equivalent permeabilities differ considerably from the laboratory measurements of equivalent permeability, which were all in the range $2\text{–}6 \times 10^{-11}$ m^2 (Fig. 4b). The modelled curves in Fig. 7a show that the equivalent permeability of a 10 m length of rock is essentially unaffected by fractures when the host rock permeability is between 10^{-13} and 10^{-11} m^2; by contrast, the addition of a single tensile fracture in low-permeability rock (between 10^{-15} and 10^{-17} m^2) increases the equivalent permeability by many orders of magnitude.

Counterintuitively, the equivalent permeability of fractured andesite does not decrease as the host rock permeability is decreased below 10^{-13} m^2. This is a consequence of the porosity dependence of the fracture permeability: fracture permeability increases as initial porosity/permeability is decreased due to the reduction in fracture tortuosity (Fig. 6). As a result, the equivalent permeability when the host rock has a permeability of 10^{-17} m^2 (highlighted in blue) is higher than that for the modelled curve at 10^{-16} m^2, which is higher than that for the 10^{-15} m^2 curve, and so on (Fig. 7a). The equivalent permeability of the 10^{-17} m^2 curve (highlighted in blue) is also higher than the 10^{-14} m^2 curve at five fractures and above (Fig. 7a).

Another way to consider the influence of lengthscale on the equivalent permeability is by increasing the considered lengthscale for a rock containing a fixed fracture number, as in Fig. 7b for a single 0.25 mm-wide fracture. We emphasise that this figure is for illustrative purposes only; in nature rock is increasingly likely to contain more than one fracture as the lengthscale is increased. Further, we highlight that our model assumes that lengthscale is shorter than the macrofracture spacing (and therefore may not be relevant for shallow rock at long lengthscales). The equivalent permeability of rock containing a single 0.25 mm-wide fracture is high (∼10^{-11} m^2) when the length considered is within the range of laboratory samples (the grey zone in Fig. 7b), regardless of the initial host rock permeability (as was the case for our laboratory measurements of equivalent permeability, see Fig. 4b). As the scale of interest increases from that considered in the laboratory (generally up to 100 mm), the equivalent permeability decreases by

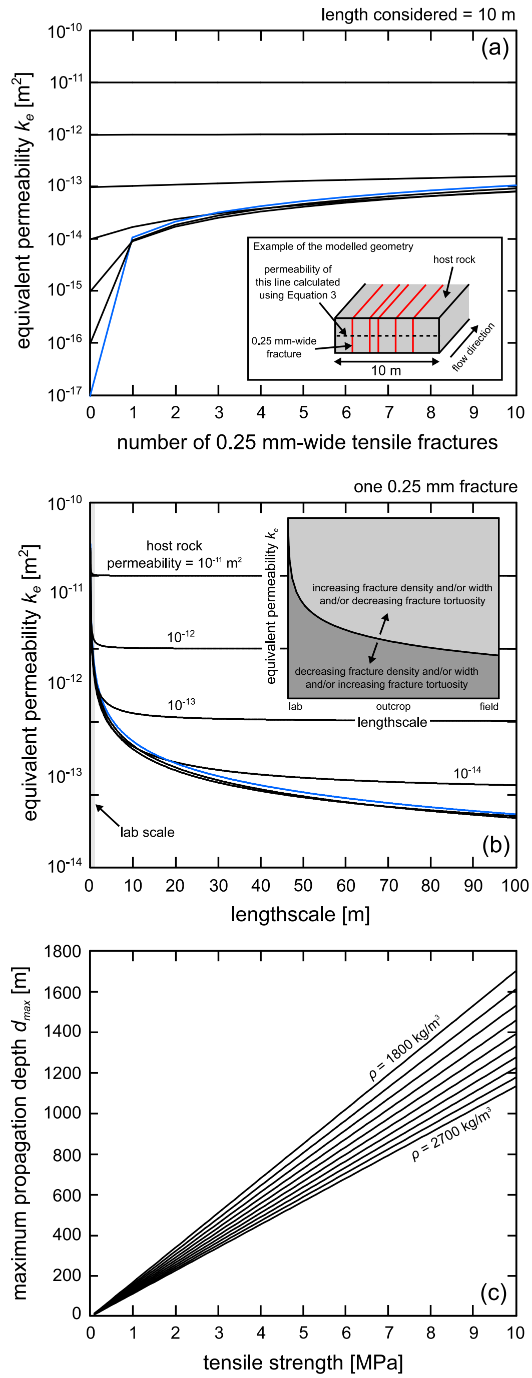

Fig. 7. (a) Equivalent permeability (k_e) of a 10 m length of rock with host rock permeabilities from 10^{-17} to 10^{-11} m^2 as a function of the number of tensile fractures (modelled using Equation (3)). Each fracture is 0.25 mm wide. Fracture permeability for each host rock was determined through the power law relationship between host rock permeability and fracture permeability. The modelled curve for a host rock permeability of 10^{-17} m^2 is highlighted in blue. The inset in panel (a) shows an example of the modelled geometry. (b) Equivalent permeability (k_e) of rock containing one 0.25 mm-wide fracture with increasing lengthscale (up to 100 m). Modelled curves (using Equation (3)) are for rock with host rock permeabilities from 10^{-17} to 10^{-11} m^2. Fracture permeability for each host rock was determined through the power law relationship between host rock permeability and fracture permeability. The laboratory scale (0 to 0.1 m) is labelled on the graph. Modelled curve for a host rock permeability of 10^{-17} m^2 is highlighted in blue. Inset shows a schematic diagram indicating the shift of the curves with increasing/decreasing fracture density, width, and tortuosity. (c) The maximum depth of a downward-propagating tensile fracture as a function of the tensile strength of the host rock, modelled for different host rock densities (from 1800 to 2700 km/m^3) using Equation (4) (from Gudmundsson, 2011). (For interpretation of the references to colour in this figure, the reader is referred to the web version of this article.)

one or more orders of magnitude when the permeability of the host rock is 10^{-12} m^2 or lower (Fig. 7b). The equivalent permeability of andesite containing one fracture, as modelled here for a lengthscale up to 100 m, is not simply a function of the host rock permeability. As discussed above, this is a result of the porosity dependence of tortuosity and therefore fracture permeability (for emphasis we again highlight the 10^{-17} m^2 curve in blue). Despite the somewhat illustrative scenario, we highlight that the equivalent permeability of a 100 m of rock is greatly influenced by one 0.25 mm-wide fracture (Fig. 7b).

We emphasise that the curves of Fig. 7b will shift towards higher equivalent permeabilities in the likely scenario where the number or width of fractures increases (and/or the fracture tortuosity decreases) with increasing lengthscale. By contrast, equivalent permeabilities will be lowered if the fracture density and/or width are decreased (and/or the fracture tortuosity is increased). This is summarised in the schematic diagram presented as an inset in Fig. 7b. As discussed above, it is increasingly likely that more fractures will be encountered at longer lengthscales. Similarly, wide fractures may also be encountered as lengthscale is increased, particularly for shallow rock or rock containing elevated pore pressures (e.g., Rust et al., 2004). Therefore, in a shallow volcanic system, the curves will be significantly shifted to higher equivalent permeabilities at long lengthscales (although we are unable to use our experimental data to explore the influence of wider fractures, the permeability of wider fractures will be higher, see Equation (1)). As the considered depth is increased, or pore pressure decreased, the increasing lithostatic pressure will decrease fracture width, and the curve will be shifted to lower equivalent permeabilities, even at long lengthscales. A final consideration is fracture tortuosity or roughness. The ability of a fracture to close at depth depends on the roughness of the fracture surface: straight or smooth fractures close more readily than rough fractures (Gavrilenko and Guéguen, 1989). Rough fractures, which could be expected for high-porosity materials, may therefore hold the potential to remain open at depth.

The approach here demonstrates how laboratory-measured permeabilities can be used to better approximate equivalent (i.e., "upscaled") permeabilities. To emphasise, if we imagine a rock outcrop (host rock permeability $= 1.0 \times 10^{-17}$ m^2) that contains 15 fractures (0.25 mm-wide) over a length of 10 m, the equivalent permeability of the rock outcrop, using a k_f of 2.18×10^{-9} m^2 (determined using the power law relationship between the initial permeability and fracture permeability), is estimated using the model presented herein to be 8.2×10^{-13} m^2. Collecting samples for laboratory measurements would therefore yield an underestimate of the permeability is the sample is pristine (the permeability of this sample would be 1.0×10^{-17} m^2) or an overestimation if the sample (length $= 0.02$ m) contains one throughgoing fracture (the equivalent permeability of this sample would be 2.7×10^{-11} m^2).

4.3. Implications for volcanic systems

The data presented herein show that a tensile fracture will have a permeability of between 10^{-10} and 10^{-9} m^2, depending on the initial porosity of the rock (Fig. 6a; Tables 1 and 2): fractures in low-porosity rock are more permeable (as high as 3.5×10^{-9} m^2) than those formed in high-porosity rock (as low as 4.1×10^{-10} m^2) due to their low tortuosity. Modelling these data shows that, at longer lengthscales, fractures greatly influence the equivalent permeability of rock with a low-permeability, but do not significant affect the equivalent permeability of rock with a high-permeability (Figs. 7a and 7b). In detail, fractured, low-permeability rock can have an equivalent permeability higher than that of similarly fractured rock with higher host rock permeability (Figs. 7a and 7b) due to the porosity dependence of tortuosity and therefore fracture permeability (Fig. 6). As a result, fractures in low-porosity, low-permeability materials—such as those at Chaitén volcano (Chile) (Castro et al., 2014)—will increase the equivalent permeability by many orders of magnitude. By contrast, tensile fractures in the porous materials at Volcán de Colima (Lavallée et al., 2016) may only increase the equivalent permeability by a factor of two or three. These data and modelling highlight an extremely important role for tensile fractures in diffusing explosive behaviour at systems dominated by low-porosity, low-permeability materials.

We note that the outgassing lifespan of these fractures depends on, amongst others, their depth and the temperature at which they reside. First, tensile fractures can partially close as a result of the overburden pressure. Nara et al. (2011) show that the permeability of a low-porosity (porosity <0.05) sample containing a macroscopic tensile fracture can be reduced by about an order of magnitude as the effective pressure is increased from 5 MPa (equivalent to a lithostatic depth of a couple of hundred m) to 50 MPa (depth $\sim$2 km). Importantly, these data show that the fracture is not completely closed even at 90 MPa (depth of $\sim$3.5–4 km). As discussed above, straight or smooth fractures close more readily than rough fractures (e.g., Gavrilenko and Guéguen, 1989). Our study has shown that tensile fractures can be more tortuous in high-porosity andesites (Fig. 6a). Therefore, we surmise that the decrease in permeability (from 5 to 50 MPa) for fractured porous materials would be less than the order of magnitude decrease in permeability seen for the low-porosity sample of Nara et al. (2011). Future experimental studies should focus on the role of confining pressure on the permeability of variably-porous rocks containing tensile fractures. Second, if the fracture resides at a temperature above Tg it can heal through the viscous sintering of the fracture surfaces or of any fragmental material within the fracture (Quane et al., 2009; Vasseur et al., 2013; Wadsworth et al., 2014; Heap et al., 2015b). However, Heap et al. (2015b) recently suggested that the slow strength recovery of sintering material could keep the conduit margins permeable through repeated fracturing. Fracture sealing/healing below Tg could occur as a result of hydrothermal mineral precipitation (Figs. 8a and 8b show sulphur deposits at active fumaroles at the edge of the lava dome at Volcán de Colima and hydrothermal precipitation within fractures at Whakaari volcano (New Zealand), respectively; see also Edmonds et al., 2003) or hot isostatic pressing (Kolzenburg et al., 2012). Therefore, either a fracture remains open and creates a pathway for fluids (which may depend on the continuous flow of fluids; Rust et al., 2004) or, and perhaps more likely, the fracture is transient and allows a "pulse" of volatiles to leave the system before succumbing to time-dependent healing or sealing by one or more of the mechanisms described above.

We also highlight here some of the constraints for extension fracture propagation. First, the length (vertically and laterally) of a propagating extension fracture can also be compromised by the presence of pre-existing discontinuities such as joints, faults, dykes, and layering (e.g., Warpinksi and Teufel, 1987; Renshaw and Pollard, 1995; Gudmundsson and Brenner, 2002). Second, downward-propagating tensile fractures will convert to a normal fault once the following relation has been satisfied (Gudmundsson, 2011):

$$d_{max} = \frac{3\sigma_t}{\rho g} \tag{4}$$

Therefore, if one assumes a typical bulk density ($\rho = 2400$ kg/m^3) and tensile strength ($\sigma_t = 3$ MPa) for porous andesite (Lavallée et al., 2016), then the maximum penetration depth for a downward-propagating tensile crack d_{max} would be 375 m (where g is the acceleration due to gravity). Once a tensile fracture converts to a shear fault, its influence on permeability will be likely governed by the porosity of the host rock (shear fractures in high-porosity rock can reduce permeability (e.g., Zhu and Wong, 1997), while shear fractures can increase the permeability of low-porosity rock (e.g., Mitchell and Faulkner, 2008). Large sub-vertical tensile fractures that propagate down from the surface are a common feature of andesitic lava domes (Fig. 8e shows a fracture adjacent to the dome at Santa María); other examples of large lava dome fractures exist at Merapi (Walter et al., 2015) and Soufrière Hills (Watts et al., 2002). However, we note that weak dome material could result in much lower penetration depths (as modelled in Fig. 7c); while there is a general paucity in tensile strength data for volcanic rocks, Heap et al. (2012) have shown that high porosity (porosity $= 0.5$) volcanic rocks can have an indirect tensile strength as low as 0.45 MPa. We further note that laboratory tensile strength measurements likely overestimate "rock mass" tensile strength (e.g., Schultz, 1996). Shallow penetration depths could provide a limit to the outgassing potential of these fractures and their ability to act as conduits from pressurised magma to the surface.

The permeable pathways formed by tensile fractures do not only allow exsolving volatiles to escape, but also permit the ingress of fluids. These fluids may be sourced from the magma, the hydrothermal system, or from the Earth's surface (glaciers or lakes). This can have two, not necessarily mutually exclusive, effects. First, if the fluids are cooler than the host material, the hot host rock cools and contracts adjacent to the fracture resulting in the formation of additional tensile fractures perpendicular to the cooling surface (i.e., the fracture) (e.g., Forbes et al., 2012). Many spectacular examples of this process exists at Mt. Ruapehu, where smaller secondary columns formed on the side of large primary cooling columns due to the rapid ingress of water (Fig. 8d; Spörli and Rowland, 2006; Conway et al., 2015). Second, the circulation of hot hydrothermal fluids can encourage the hydrothermal alteration of the host rock and/or further tensile fracturing through the build-up of fluid overpressures. Since hydrothermally-altered rocks are generally weaker than pristine rock (Pola et al., 2014; Wyering et al., 2014; Heap et al., 2015c), alteration can also lead to further fracturing. Examples of intense hydrothermal alteration and mineral precipitation can be seen in the fractured andesites at Pinnacle Ridge on Mt. Ruapehu (Figs. 8f and 8g; Hackett and Houghton, 1989) and in fractured lavas at Whakaari volcano (Fig. 8b; Heap et al., 2015c).

5. Concluding remarks

The permeability of a volcanic system is expected to impact explosivity: low-permeability rocks and magma can allow the pore pressure to build to that preparatory for an explosive eruption (e.g., Sparks, 1997; Melnik et al., 2005), while high-permeability rocks and magma will permit outgassing, compaction, and encourage quiescence (Kennedy et al., 2015). Extension fractures at volcanoes are expected to play an important role in outgassing (e.g., Stasiuk et al., 1996; Castro et al., 2014), although laboratory permeability data on volcanic rocks are scarce (e.g., Nara et al., 2011; Heap et al., 2015a). Our experimental and modelling approach offers some novel insights. First, we find here that, irrespective of the initial porosity, a single fracture in a laboratory sample (in which the fracture plane is parallel to the flow direction) will result in a permeability of between 2–6 $\times$ 10^{-11} m^2. Second, that the permeability of a fracture is influenced by the initial porosity and pore size of the rock: the more heterogeneous the rock, the more tortuous the resultant tensile fracture, and the lower the fracture permeability. Third, when these data are used to model the equivalent permeability of fractured rock, we find that equivalent permeability depends heavily on the scale of interest and the initial permeability of the host rock. Our modelling highlights that the equivalent permeability of a low-permeability rock is greatly increased upon the formation of a single fracture, while the equivalent permeability of high-permeability rock is largely unaffected

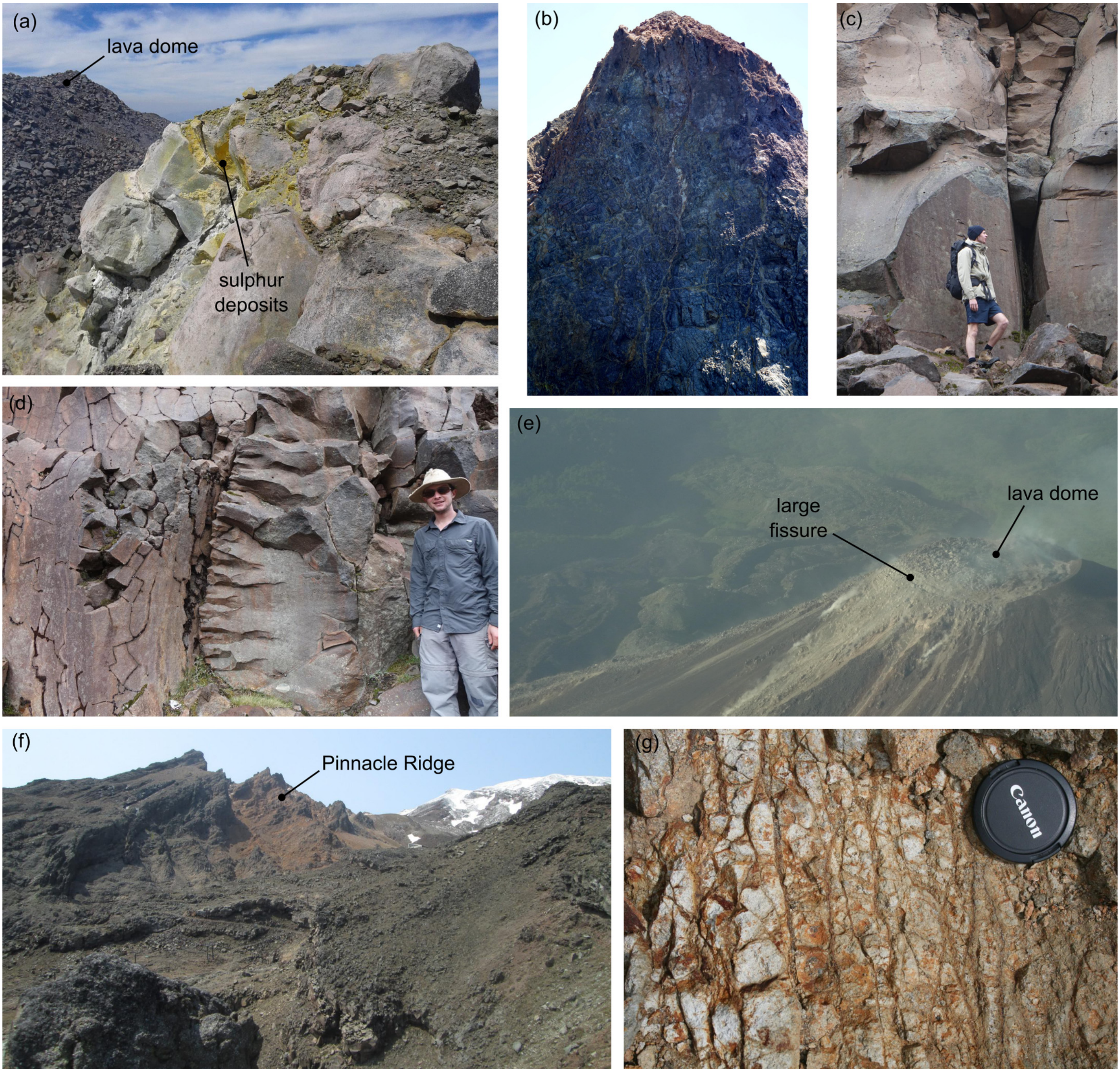

Fig. 8. Field photographs. (a) Photograph of sulphur deposits near a fumarole next to the dome at Volcán de Colima (Mexico) on March 2012 (photo credit: Jamie Farquharson). Photograph of the highly fractured and altered host rock at Whakaari volcano (New Zealand) (photo credit: Ben Kennedy). (c) Photograph of large fractures in the andesite of the Whakapapa Formation (Ruapehu, New Zealand) (photo credit: Ben Kennedy). Chris Conway for scale. (d) Photograph of column-on-column cooling fractures in the andesite of the Whakapapa Formation (Ruapehu) (photo credit: Ben Kennedy). Stan Mordensky for scale. (e) Photograph of the lava dome at Santa María (Guatemala) in 2012 (photo credit: Ben Kennedy). (f) View of Pinnacle Ridge on Mt. Ruapehu (New Zealand) (photo credit: Michael Heap). (g) Photograph of the highly fractured and altered host rock at Pinnacle Ridge (photo credit: Ben Kennedy).

by the presence of many fractures. We also find that fractured, low-permeability rock (e.g., 10^{-17} m^2) can have an equivalent permeability higher than that of similarly fractured rock with higher host rock permeability (e.g., 10^{-15} m^2) due to the porosity dependence of fracture tortuosity and therefore permeability. The modelling therefore highlights an important role for extension fractures in outgassing low-porosity and low-permeability volcanic systems. While our laboratory measurements show that, regardless of the initial porosity, the equivalent permeability of fractured rock on the laboratory scale is 2–6 $\times$ 10^{-11} m^2, the equivalent permeability of low-permeability rock containing a single fracture is significantly reduced as the scale of interest is increased. We find that this role of lengthscale on equivalent permeability diminishes for high-permeability rocks. In summary, due to the scale-dependence of permeability, laboratory measurements on pristine rocks significantly underestimate the equivalent permeability of a fractured volcanic system, and measurements on fractured rocks can significantly overestimate the equivalent permeability. As a result, care must be taken when selecting representative samples from the field for laboratory experiments and input parameters for volcano outgassing models (e.g., Collombet, 2009; Collinson and Neuberg, 2012). We highlight that our modelling approach can be used to estimate the equivalent permeability of numerous scenarios at andesitic stratovolcanoes in which the fracture density and width and host rock porosity or permeability are known.

Acknowledgements

The authors thank Paul Siratovich at Mighty River Power for field assistance and discussions. The first author would like to additionally thank Jamie Farquharson, Luke Griffiths, Hugh Tuffen, Alex Kushnir, Patrick Baud, Olivier Lengliné, and Thierry Reuschlé. Gilles Morvan is thanked for his assistance using the SEM. Special thanks to Harry Keys and Blake McDavitt at the New Zealand Department of Conservation, Ngati Tuwharetoa, Ngati Rangi, and Ruapehu Alpine Lifts for providing access to and permission to sample at Ruapehu. The authors of this study acknowledge a Dumont d'Urville grant (number 31950RK) Hubert Curien Partnership (PHC) grant, funded and implemented by the New Zealand Ministry of Business, Innovation and Employment (MBIE), the Royal Society of New Zealand, and the Ministry of Foreign Affairs (MAEDI) and the Ministry of Higher Education and Research (MENESR) in France. The first author acknowledges funding from an Initiative d'Excellence (IDEX) "Attractivité" grant (VOLPERM), funded by the University of Strasbourg. This work has been published under the framework of LABEX grant ANR-11-LABX-0050_G-EAU-THERMIE-PROFONDE and therefore benefits from state funding managed by the Agence Nationale de la Recherche (ANR) as part of the "Investissements d'avenir" program. The comments of three anonymous reviewers helped improve this manuscript.

References

Anderson, S.W., Fink, J.H., 1992. Crease structures: indicators of emplacement rates and surface stress regimes of lava flows. Bull. Geol. Soc. Am. 104, 615–625.
Aydin, A., DeGraff, J.M., 1988. Evolution of polygonal fracture patterns in lava flows. Science 239, 471–476.
Benson, P.M., Heap, M.J., Lavallée, Y., Flaws, A., Hess, K.-U., Selvadurai, A.P.S., Dingwell, D.B., Schillinger, B., 2012. Laboratory simulations of tensile fracture development in a volcanic conduit via cyclic magma pressurisation. Earth Planet. Sci. Lett. 349–350, 231–239.
Brace, W.F., 1984. Permeability of crystalline rocks: new in situ measurements. J. Geophys. Res. 89, 4327–4330.
Brown, S.R., 1987. Fluid flow through rock joints: the effect of surface roughness. J. Geophys. Res. 92, 1337–1347.
Castro, J., Bindeman, I.N., Tuffen, H., Schipper, C.I., 2014. Explosive origin of silicic lava: textural and δD–H_2O evidence for pyroclastic degassing during rhyolite effusion. Earth Planet. Sci. Lett. 405, 52–61.
Clauser, C., 1992. Permeability of crystalline rocks. Earth Space Sci. News 73, 233–238.
Collinson, A.S.D., Neuberg, J., 2012. Gas storage, transport and pressure changes in an evolving permeable volcanic edifice. J. Volcanol. Geotherm. Res. 243–244, 1–13.
Collombet, M., 2009. Two-dimensional gas loss for silicic magma flows: toward more realistic numerical models. Geophys. J. Int. 177, 309–318.
Conway, C.E., Townsend, D.B., Leonard, G.S., Wilson, C.J.N., Calvert, A.T., Gamble, J.A., 2015. Lava–ice interaction on a large composite volcano: a case study from Ruapehu, New Zealand. Bull. Volcanol. 77 (21).
Deer, W.A., Howie, R.A., Zussman, J., 1992. An Introduction to the Rock-Forming Minerals. Longman Scientific and Technical, Harlow.
Dingwell, D.B., Webb, S.L., 1990. Relaxation in silicate melts. Eur. J. Mineral. 2, 427–449.
Edmonds, M., Oppenheimer, C., Pyle, D.M., Herd, R.A., Thompson, G., 2003. SO_2 emissions from Soufrière Hills Volcano and their relationship to conduit permeability, hydrothermal interaction and degassing regime. J. Volcanol. Geotherm. Res. 124, 23–43.
Edmonds, M., Herd, R.A., 2007. A volcanic degassing event at the explosive–effusive transition. Geophys. Res. Lett. 37 (21). http://dx.doi.org/10.1029/2007GL031379.
Eichelberger, J.C., Carrigan, C.R., Westrich, H.R., Price, P.H., 1986. Non-explosive silicic volcanism. Nature 323, 598–602.
Farquharson, I.J., Heap, M.J., Varley, N., Baud, P., Reuschlé, T., 2015. Permeability and porosity relationships of edifice-forming andesites: a combined field and laboratory study. J. Volcanol. Geotherm. Res. 297, 52–68.
Fitzgerald, R.H., Tsunematsu, K., Kennedy, B.M., Breard, E.C.P., Lube, G., Wilson, T.M., Jolly, A.D., Pawson, J., Rosenberg, M.D., Cronin, S.J., 2014. The application of a calibrated 3D ballistic trajectory model to ballistic hazard assessments at Upper Te Maari, Tongariro. J. Volcanol. Geotherm. Res. 286, 248–262.
Forbes, A.E.S., Blake, S., McGarvie, D.W., Tuffen, H., 2012. Pseudopillow fracture systems in lavas: insights into cooling mechanisms and environments from lava flow fractures. J. Volcanol. Geotherm. Res. 245–246, 68–80.
Gavrilenko, P., Guéguen, Y., 1989. Pressure dependence of permeability: a model for cracked rocks. Geophys. J. Int. 98, 159–172.
Gudmundsson, A., 2011. Rock Fractures in Geological Processes. Cambridge University Press, Cambridge.
Gudmundsson, A., Brenner, S.L., 2002. How hydrofractures become arrested. Terra Nova 13, 456–462.
Gudmundsson, A., Fjeldskaar, I., Brenner, S.L., 2002. Propagation pathways and fluid transport of hydrofractures in jointed and layered rocks in geothermal fields. J. Volcanol. Geotherm. Res. 116, 257–278.
Hackett, W.R., Houghton, B.F., 1989. A facies model for a quaternary andesitic composite volcano, Ruapehu, New Zealand. Bull. Volcanol. 51, 51–68.
Heap, M.J., Lavallée, Y., Laumann, A., Hess, K.-U., Meredith, P.G., Dingwell, D.B., 2012. How tough is tuff in the event of fire? Geology 40, 311–314.
Heap, M.J., Lavallée, Y., Petrakova, L., Baud, P., Reuschlé, T., Varley, N., Dingwell, D.B., 2014. Microstructural controls on the physical and mechanical properties of edifice-forming andesites at Volcán de Colima, Mexico. J. Geophys. Res. 119, 2925–2963.
Heap, M.J., Farquharson, I.J., Baud, P., Lavallée, Y., Reuschlé, T., 2015a. Fracture and compaction of andesite in a volcanic edifice. Bull. Volcanol. 77, 55. http://dx.doi.org/10.1007/s00445-015-0938-7.
Heap, M.J., Farquharson, I.J., Wadsworth, F.B., Kolzenburg, S., Russell, J.K., 2015b. Timescales for permeability reduction and strength recovery in densifying magma. Earth Planet. Sci. Lett. 429, 223–233.
Heap, M.J., Kennedy, B.M., Pernin, N., Jacquemard, L., Baud, P., Farquharson, I.J., Scheu, B., Lavallée, Y., Gilg, H.A., Letham-Brake, M., Mayer, K., Jolly, A.D., Reuschlé, T., Dingwell, D.B., 2015c. Mechanical behaviour and failure modes in the Whakaari (White Island volcano) hydrothermal system, New Zealand. J. Volcanol. Geotherm. Res. 295, 26–42.
Heiken, G., Wohletz, K., Eichelberger, J.C., 1988. Fracture fillings and intrusive pyroclasts, Inyo Domes, California. J. Geophys. Res. 93, 4335–4350.
Jaeger, J., Cook, N.G.W., Zimmerman, R., 2007. Fundamentals in Rock Mechanics, 4th edition. Blackwell Publishing, London.
Kennedy, B.M., Spieler, O., Scheu, B., Kueppers, U., Taddeucci, J., Dingwell, D.B., 2005. Conduit implosion during vulcanian eruptions. Geology 33 (7), 581–584.
Kennedy, B.M., Wadsworth, F.B., Vasseur, J., Schipper, C.I., Jellinek, A.M., von Aulock, F.W., Hess, K.-U., Russell, J.K., Lavallée, Y., Nichols, A.R.L., Dingwell, D.B., 2015. Surface tension driven processes densify and retain permeability in magma and lava. Earth Planet. Sci. Lett. 433, 116–124.
Knapp, R.B., Knight, J.E., 1977. Differential thermal expansion of pore fluids: fracture propagation and microearthquake production in hot pluton environments. J. Geophys. Res. 82, 2515–2522.
Kolzenburg, S., Heap, M.J., Lavallée, Y., Russell, J.K.R., Meredith, P.G., Dingwell, D.B., 2012. Strength and permeability recovery of tuffisite-bearing andesite. Solid Earth 3, 191–198.
Kushnir, A.R.L., Martel, C., Bourdier, J.-L., Heap, M.J., Reuschlé, T., Erdmann, S., Komorowski, J.C., Cholik, N., 2016. Probing permeability and microtexture: unravelling the role of a low-permeability dome on the explosivity of Merapi (Indonesia). http://dx.doi.org/10.1016/j.jvolgeores.2016.02.012.
Lavallée, Y., Varley, N., Alatorre-Ibargüengoitia, M.A., Hess, K.-U., Kueppers, U., Mueller, S., Richard, D., Scheu, B., Spieler, O., Dingwell, D.B., 2012. Magmatic architecture of dome-building eruptions at Volcán de Colima, Mexico. Bull. Volcanol. 74, 249–260.
Lavallée, Y., Benson, P.M., Heap, M.J., Hess, K.-U., Flaws, A., Schillinger, B., Meredith, P.G., Dingwell, D.B., 2013. Reconstructing magma failure and the degassing network of dome-building eruptions. Geology 41, 515–518.
Lavallée, Y., Heap, M.J., Kueppers, U., Kendrick, J.E., Dingwell, D.B., 2016. The fragility of Volcán de Colima—a material constraint. In: Varley, N., Komorowski, J.C. (Eds.), Volcán de Colima: Managing the Threat. Springer-Verlag, Berlin, Heidelberg.
Melnik, O., Barmin, A.A., Sparks, R.S.J., 2005. Dynamics of magma flow inside volcanic conduits with bubble overpressure buildup and gas loss through permeable magma. J. Volcanol. Geotherm. Res. 143, 53–68.
Mitchell, T.M., Faulkner, D.R., 2008. Experimental measurements of permeability evolution during triaxial compression of initially intact crystalline rocks and implications for fluid flow in fault zones. J. Geophys. Res. 113 (B11). http://dx.doi.org/10.1029/2008JB005588.
Mueller, S., Melnik, O., Spieler, O., Scheu, B., Dingwell, D.B., 2005. Permeability and degassing of dome lavas undergoing rapid decompression: an experimental study. Bull. Volcanol. 67, 526–538.
Nara, Y., Meredith, P.G., Yoneda, T., Kaneko, K., 2011. Influence of macro-fractures and micro-fractures on permeability and elastic wave velocities in basalt at elevated pressure. Tectonophysics 503, 52–59.
Neuman, S.P., 1994. Generalized scaling of permeabilities: validation and effect of support scale. Geophys. Res. Lett. 21, 349–352.

Pola, A., Crosta, G.B., Fusi, N., Castellanza, R., 2014. General characterization of the mechanical behaviour of different volcanic rocks with respect to alteration. Eng. Geol. 169, 1–13.

Quane, S.L., Russell, J.K., Friedlander, E.A., 2009. Time scales of compaction in volcanic systems. Geology 37, 471–474.

Renard, P., de Marsily, G., 1997. Calculating equivalent permeability: a review. Adv. Water Resour. 20, 253–278.

Renshaw, C.E., Pollard, D.D., 1995. An experimentally verified criterion for propagation across unbounded frictional interfaces in brittle, linear elastic materials. Int. J. Rock Mech. Min. Sci. Geomech. Abstr. 32, 237–249.

Rust, A., Cashman, K.V., 2004. Permeability of vesicular silicic magma: inertial and hysteresis effects. Earth Planet. Sci. Lett. 228, 93–107.

Rust, A.C., Cashman, K.V., Wallace, P.J., 2004. Magma degassing buffered by vapor flow through brecciated conduit margins. Geology 32, 349–352.

Schultz, R.A., 1996. Relative scale and the strength and deformability of rock masses. J. Struct. Geol. 18, 1139–1149.

Sparks, R.S.J., 1997. Causes and consequences of pressurisation in lava dome eruptions. Earth Planet. Sci. Lett. 150, 177–189.

Spörli, K.B., Rowland, J.V., 2006. 'Column on column' structures as indicators of lava/ice interaction, Ruapehu andesite volcano, New Zealand. J. Volcanol. Geotherm. Res. 157, 297–310.

Stasiuk, M.V., Barclay, J., Carroll, M.R., Jaupart, C., Ratté, J.C., Sparks, R.S.J., Tait, S.R., 1996. Degassing during magma ascent in the Mule Creek vent (USA). Bull. Volcanol. 58, 117–130.

Thompson, M.E., Brown, S.R., 1991. The effect of anisotropic surface roughness on flow and transport in fractures. J. Geophys. Res. 96, 21923–21932.

Tuffen, H., Dingwell, D.B., 2005. Fault textures in volcanic conduits: evidence for seismic trigger mechanisms during silicic eruptions. Bull. Volcanol. 67, 370–387.

Ulusay, R., Hudson, J.A., 2007. The Complete ISRM Suggested Methods for Rock Characterization, Testing and Monitoring: 1974–2006. International Society for Rock Mechanics, ISBN 978-975-93675-4-1. 628 pp.

Vasseur, J., Wadsworth, F.B., Lavallée, Y., Hess, K.-U., Dingwell, D.B., 2013. Volcanic sintering: timescales of viscous densification and strength recovery. Geophys. Res. Lett. 40, 5658–5664.

Voight, B., 2000. Structural stability of andesite volcanoes and lava domes. Philos. Trans. R. Soc., Math. Phys. Eng. Sci. 358 (1770), 1663–1703. Causes and consequences of eruptions of andesite volcanoes (May 15, 2000), 1663–1703.

Wadsworth, F.B., Vasseur, J., von Aulock, F.W., Hess, K.-U., Scheu, B., Lavallée, Y., Dingwell, D.B., 2014. Nonisothermal viscous sintering of volcanic ash. J. Geophys. Res. 119, 8792–8804.

Walter, T.R., Subandriyo, J., Kirbani, S., Bathke, H., Suryanto, W., Aisyah, N., Darmawan, H., Jousset, P., Luehr, B.-G., Dahm, T., 2015. Volcano-tectonic control of Merapi's lava dome splitting: the November 2013 fracture observed from high resolution TerraSAR-X data. Tectonophysics 639, 23–33.

Warpinksi, N.R., Teufel, L.W., 1987. Influence of geologic discontinuities on hydraulic fracture propagation. J. Pet. Technol. 39. http://dx.doi.org/10.2118/13224-PA.

Watts, R.B., Herd, R.A., Sparks, R.S.J., Young, S.R., 2002. Growth patterns and emplacement of the andesitic lava dome at Soufrière Hills Volcano, Montserrat. Mem. Geol. Soc. Lond. 21, 115–152. http://dx.doi.org/10.1144/GSL.MEM.2002.021.01.06.

Wright, H.M.N., Roberts, J.J., Cashman, K.V., 2006. Permeability of anisotropic tube pumice: model calculations and measurements. Geophys. Res. Lett. 33. http://dx.doi.org/10.1029/2006GL027224.

Wyering, L.D., Villeneuve, M.C., Wallis, I.C., Siratovich, P., Kennedy, B., Gravely, D.M., Cant, J.L., 2014. Mechanical and physical properties of hydrothermally altered rocks, Taupo Volcanic Zone, New Zealand. J. Volcanol. Geotherm. Res. 288, 76–93.

Zhu, W., Wong, T.-f., 1997. The transition from brittle faulting to cataclastic flow: permeability evolution. J. Geophys. Res. 102 (B2), 3027–3041.

Zimmerman, R.W., Chen, D.-W., Cook, N.W.G., 1992. The effect of contact area on the permeability of fractures. J. Hydrol. 139, 79–96.

Zimmerman, R.W., Bodvarsson, G.S., 1996. Hydraulic conductivity of rock fractures. Transp. Porous Media 23, 1–30.